Radar Observations of Mesovortices Associated with the Second 30 June – 1 July 2014 Midwestern Derecho

Anthony W. Lyza, Adam W. Clayton, and Kevin R. Knupp
Severe Weather Institute – Radar and Lightning Laboratories
University of Alabama in Huntsville, Huntsville, AL

Eric Lenning, Richard Castro, and Matthew Friedlein
NOAA/NWS Chicago, IL

Evan Bentley
NOAA/NWS Syracuse, IN

1. Introduction

A significant severe weather episode impacted portions of the Midwestern United States from the midday hours of 30 June through the predawn hours of 1 July 2014. The event, officially classified as two derechos (NWS Chicago 2015), began as a series of supercells merged into a progressive derecho across western and central Iowa during the midday hours of 30 June and moved eastward, producing widespread wind damage across Iowa, northern Illinois, and southern Wisconsin, along with eight confirmed tornadoes (Fig. 1; Storm Prediction Center 2015). As the first derecho began to dissipate across northern Indiana and southern Lower Michigan, a secondary quasi-linear convective system (QLCS) began to form approximately 250 km behind the first derecho. As this QLCS moved into north-central Illinois, it intensified into a second derecho and began to produce widespread wind damage and at least 29 tornadoes (Fig. 2; Storm Prediction Center 2015), with many additional tornadoes suspected. All of the tornadoes and much of the wind damage were associated with any of 39 detected mesovortices (Fig. 2), defined in this case as vortices found along the leading edge of a QLCS and generally 2 km to 10 km in diameter (e.g. Weisman and Trapp 2003, Wakimoto et al. 2006, Wheatley and Trapp 2008, Atkins and St. Laurent 2009a). Some of the vortices in this case were slightly below 2 km in diameter, more in-line with the definition of a misovortex (Fujita 1981), although all of these similar vortices are referred to as mesovortices in this work for the sake of clarity. At one point during the second derecho, at least 15 mesovortices were identified occurring simultaneously (Fig. 3). More information on the meteorological conditions that promoted the second derecho can be found in proceedings by Friedlein et al. (2015) and Lenning et al. (2015).

This presentation focuses on the mesovortices of the second 30 June – 1 July 2014 Midwestern derecho. The presence of two Weather Surveillance Radar – 88 Doppler (WSR-88D) radars and two terminal Doppler weather radars (TDWRs) and the prolific mesovortex generation of the second derecho allowed for a number of remarkable observations of mesovortex behavior. These observations include, but are not limited to, the following:

1. Splitting of one large mesovortex into two subvortices, followed by prolific tornado production;
2. Satellite behavior of three mesovortices around one larger mesovortex; and
3. The merging of up to four distinct tornado debris signatures (TDSs; e.g. Ryzhkov et al. 2005, Schultz et al. 2012a,b) into one large, elongated signature of debris.

This paper overviews these observed behaviors and places them into context with previous research on QLCS mesovortices. Research and operational questions are addressed.

2. The Splitting of Mesovortex G and Properties of the Resulting Subvortices

One of the most damaging occurrences during the second derecho of 30 June – 1 July 2014 was associated with a long-lived mesovortex that moved across northeastern Illinois and northwestern Indiana (Fig. 4). This mesovortex, hereafter known as "mesovortex 'G'" using the naming scheme developed for this case, initially developed in the far southwestern suburbs of Chicago, Illinois, at around 0248 UTC 1 July (Fig. 5). As the mesovortex moved to the southeast, it continued to grow in size (Fig. 6) until it began to split into two subvortices (Fig. 7; hereafter G-1 for the northern subvortex and G-2 for the southern subvortex). Subvortex G-1 began to produce tornadoes at approximately 0325 UTC, while

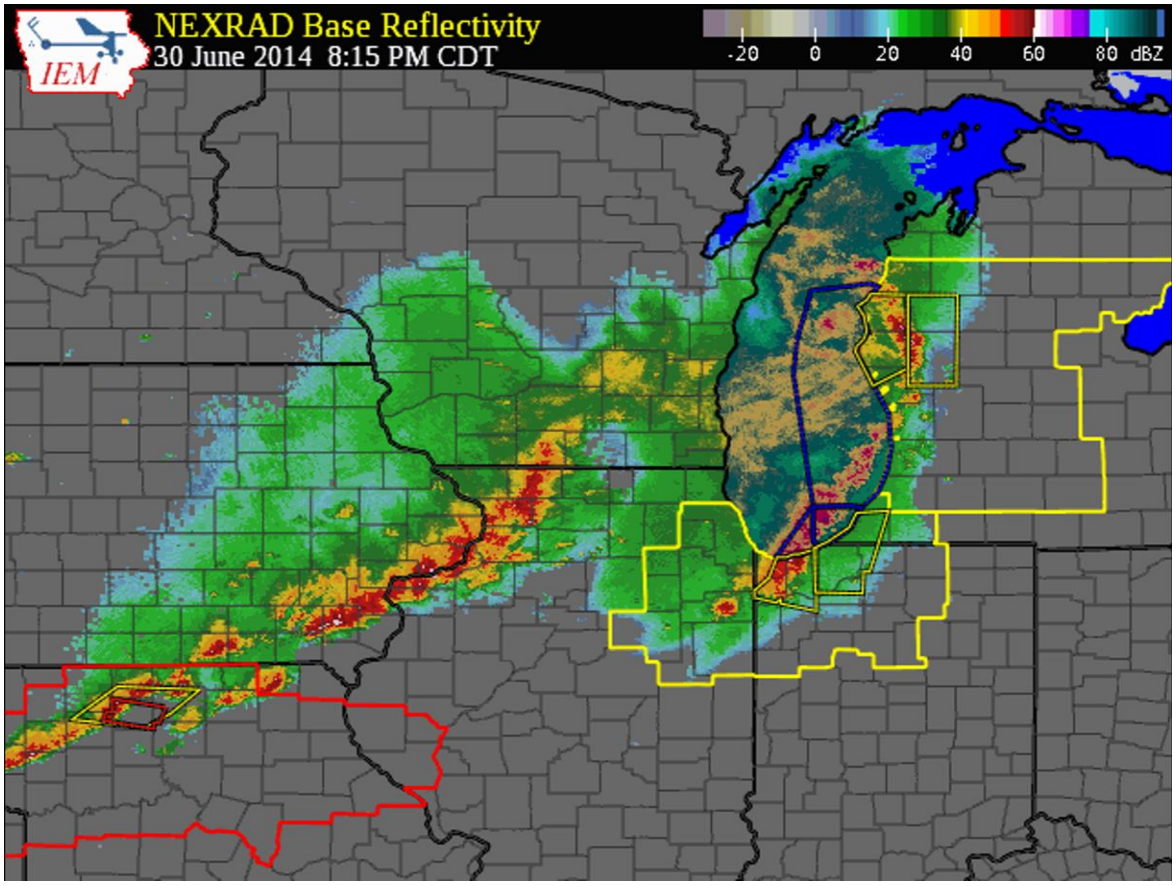

Fig. 1: Overview radar image of the two 30 June - 1 July 2014 derechos.

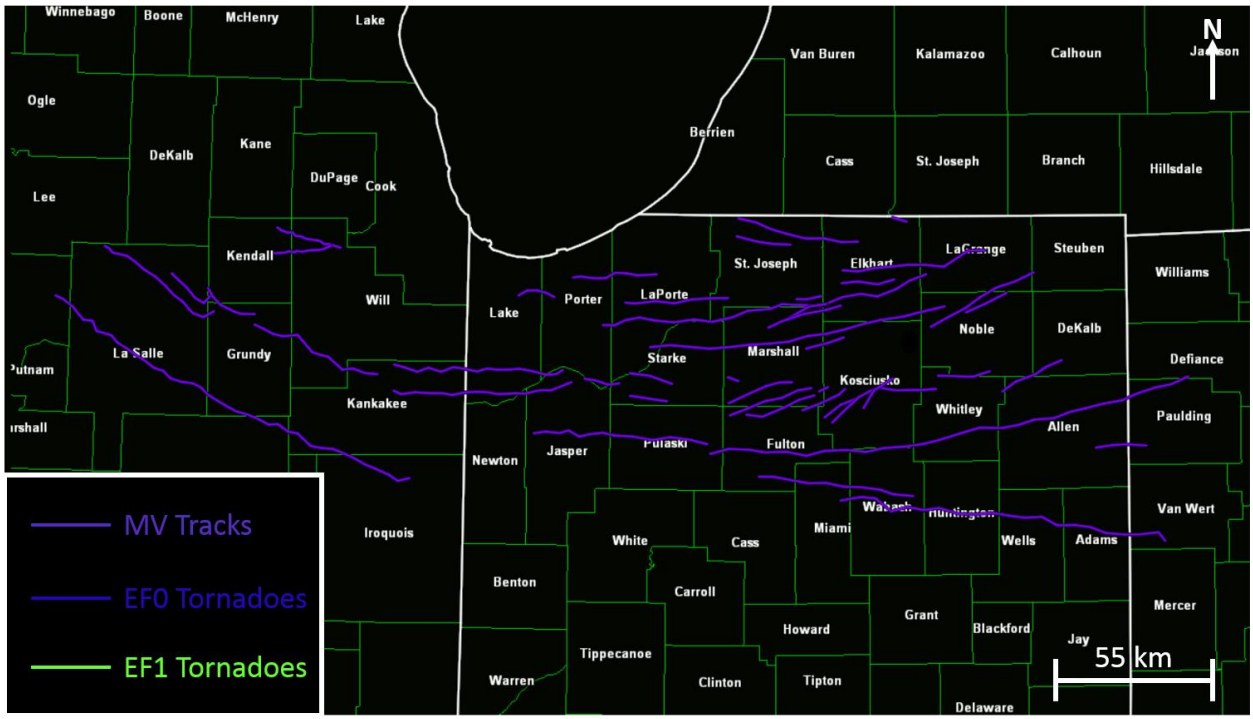

Fig. 2: Overview animation of mesovortex and tornado tracks from the second derecho. Click here to animate back and forth between mesovortex and tornado tracks.

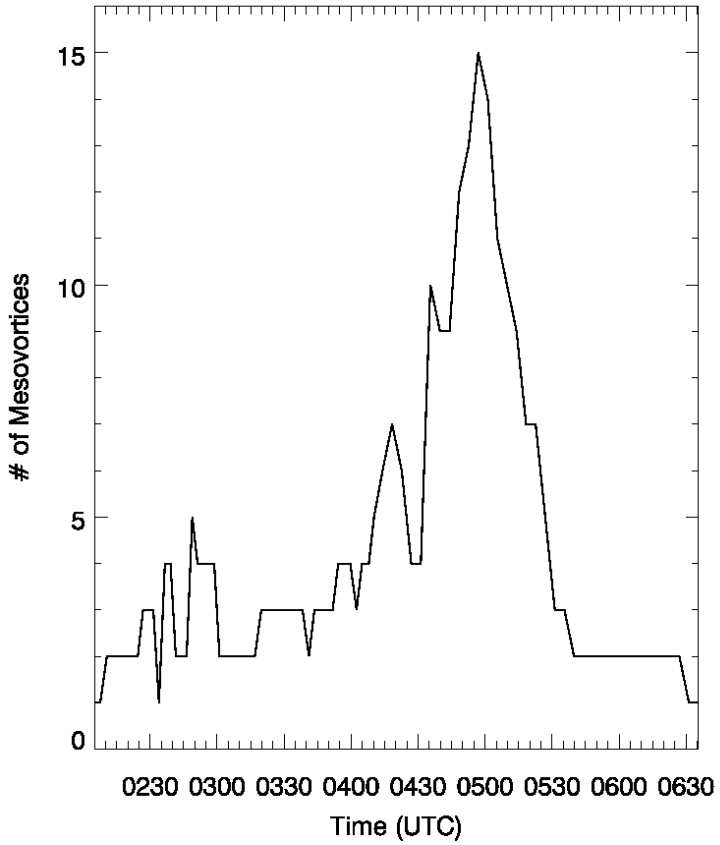

Fig. 3: Time series of simultaneous ongoing mesovortices during the second derecho.

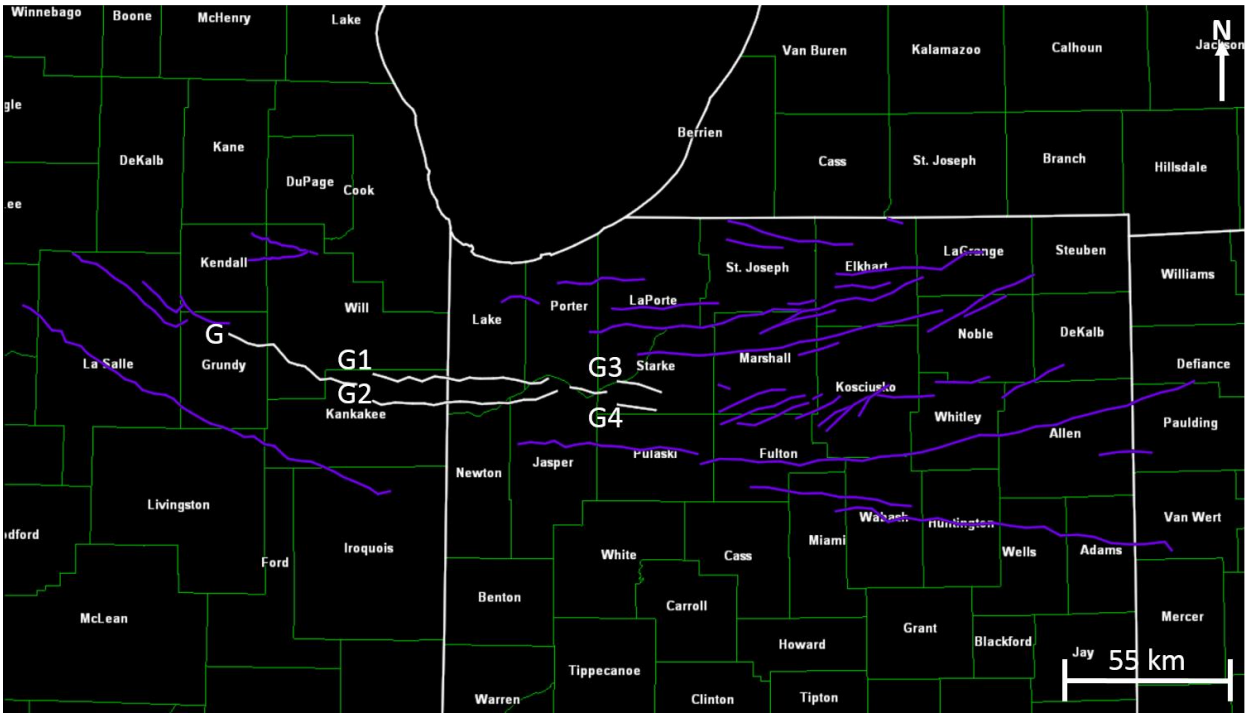

Fig. 4: Overview map showing the location of mesovortex G in context to all the mesovortices of the second derecho.

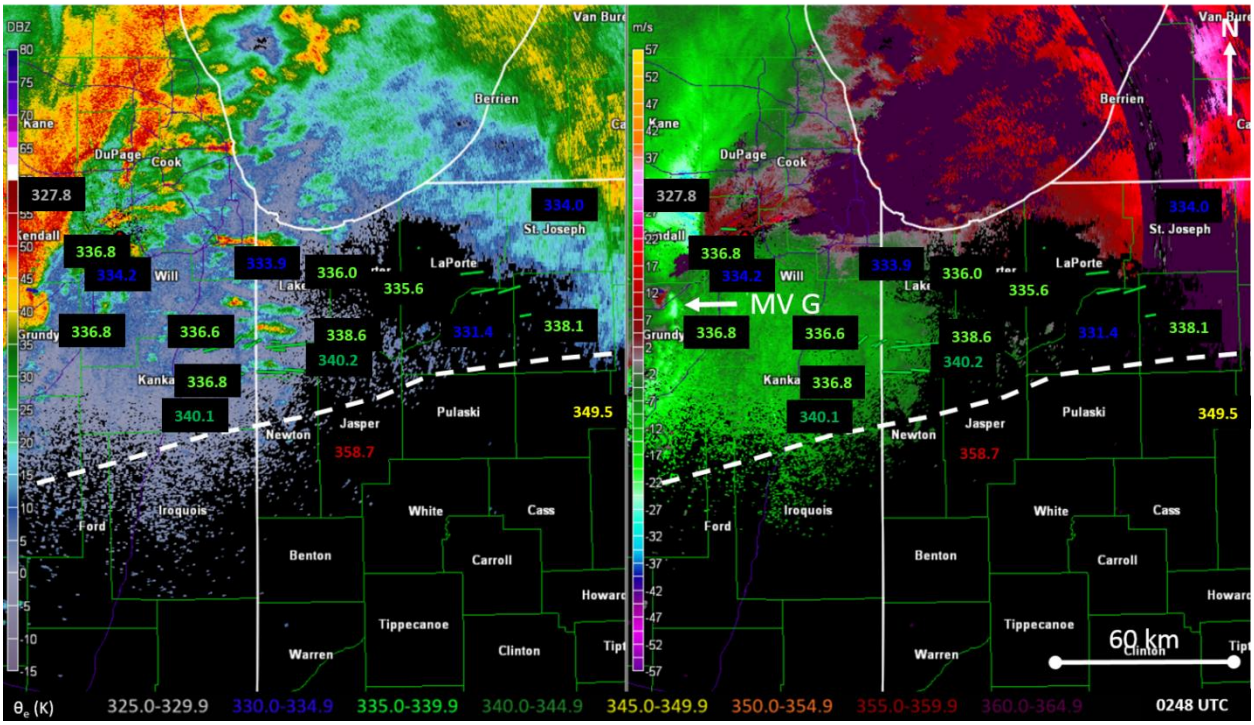

Fig. 5: 0.5° plan position indicator (PPI) plot of equivalent reflectivity factor (Z_e, left) and radial velocity (V_r, right) from the Chicago/Romeoville, Illinois (KLOT) WSR-88D at 0248 UTC 1 July 2014. Overlaid numbers indicate equivalent potential temperature (θ_e, K), while the white dashed line indicates the approximate position of the thermal boundary left by the first derecho. Green lines indicate EF1 tornado tracks. Mesovortex G had just formed at this time and is denoted above.

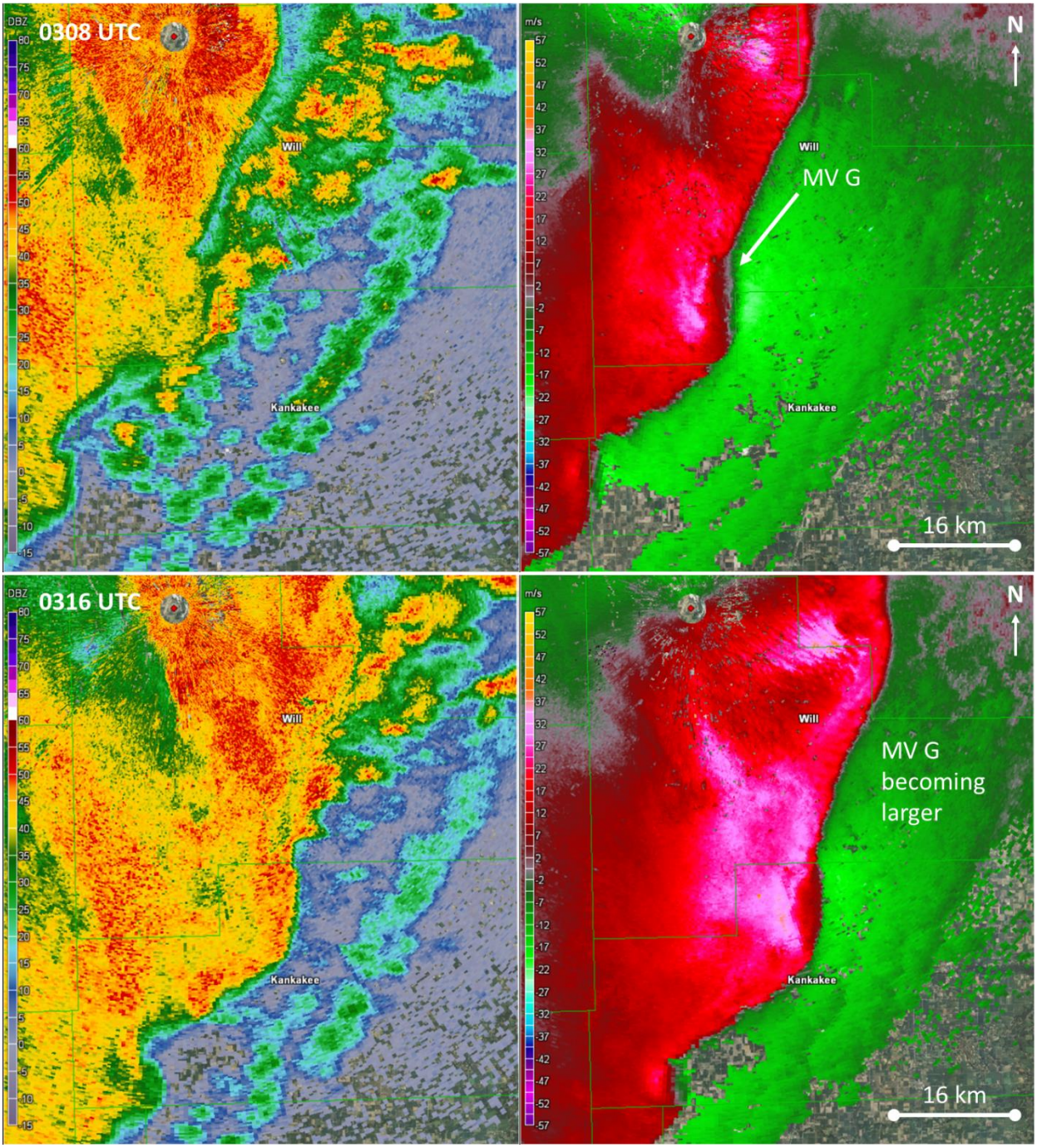

Fig. 6: 0.5° PPI of Z_e (left) and V_r (right) at 0308 UTC (top) and 0316 UTC (bottom) on 1 July 2014 from the KLOT WSR-88D, showing the growth of mesovortex G over time.

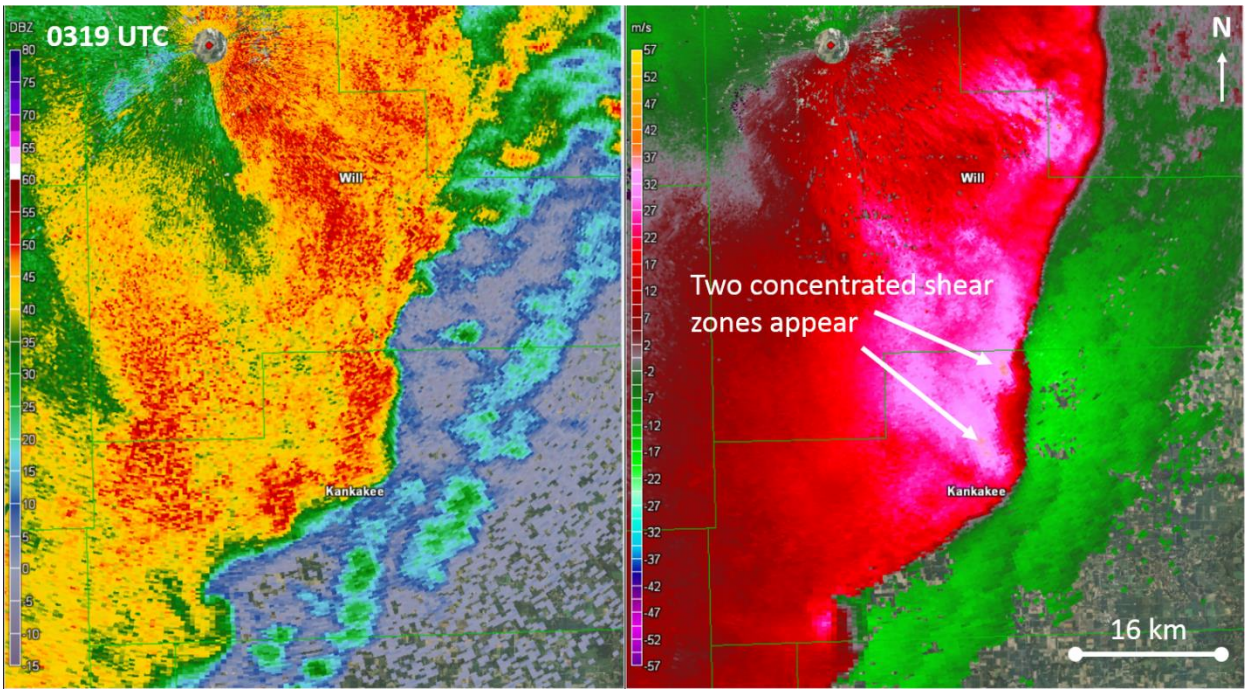

Fig. 7: As in Fig. 6 at 0319 UTC on 1 July 2014, showing the split of mesovortex G.

the southern subvortex became tornadic at approximately 0329 UTC (Fig. 8, Storm Prediction Center 2015). In all, G-1 was associated with 8 tornadoes, while G-2 was associated with 6 confirmed tornadoes. In addition to the tornado tracks, G-1 was responsible for a wide swath of wind damage estimated at up to near-EF2 intensity on the Enhanced Fujita Scale (McDonald et al. 2004). As shown in Fig. 8, the two subvortices were initially similar in intensity and in size as they first began to produce tornadoes. However, as the second derecho continued to propagate eastward, G-1 propagated along a retreating remnant thermal boundary from the first derecho (Figs. 5 and 9). This thermal boundary was extremely well-defined at the surface, with a maximum equivalent potential temperature (θe) change of 10.6 K over a distance of 9.2 km (Fig. 10). Increased convergence and vorticity stretching has been found to be a substantial factor in mesovortex intensification in mesovortices propagating along thermal boundaries, with smaller contributions due to baroclinic vorticity generation and horizontal wind shear (Wheatley and Trapp 2008).

The position of G-1 along the thermal boundary appeared to have a direct effect on its evolution when compared to the evolution of nearby subvortex G-2. As stated previously, the two subvortices appeared to be nearly equal when mesovortex G initially splits (Figs. 7 and 8), but by the time G-1 and G-2 reach the cooperative observer sites in northwest Indiana (Fig. 10), G-1 is clearly larger and more intense than G-2. And although both G-1 and G-2 were prolific tornado producers, only G-1 was associated with a large swath of wind damage estimated at 45 m s-1 or higher in damage surveys by the lead author and the fifth author. The differences in evolution between G-1 and G-2 are shown in Fig. 11. For the entirety of its lifespan, the circulation of G-1 was detectable up to a minimum at least 6 km deep and a maximum of nearly 9 km deep. Though this depth is not unprecedented (Weisman and Trapp 2003), such mesovortices are more commonly lower-tropospheric phenomena, with maximum depths of approximately 3 km (e.g. Atkins et al. 2004). The depth of G-2 was approximately 3-4 km AGL during its lifespan, a more typical range of maximum depth of a leading-edge mesovortex. Without a dual-Doppler or synthetic dual-Doppler synthesis able to be performed, much uncertainty remains as to whether or not the detected depth of G-1 is due to the circulation attaining supercell mesocyclone characteristics, the chance superposition of a mid-level and low-level mesovortex, or a chance, persistent radar detection artifact (though the latter seems unlikely). A cross-section of equivalent reflectivity factor (Z_e) shows a distinct peak in the depth of intense (> 40 dBZ) Z_e echoes in the vicinity of G-1 (Fig. 12), further tentatively supporting the notion of this region of the line having gained supercell-like characteristics, although a rear-inflow jet (RIJ) was also prominent in radar observations of this portion of the line (not shown). The relative intensity of G-1 versus G-2 is also noted in the time-series of rotational velocity

(V_{ROT}), which shows a simultaneous increase in V_{ROT} for G-1 and decrease for G-2 after 0340 UTC (Fig. 11). The diameter of G-1 was also greater than the diameter of G-2 after 0340 UTC, which led to a small net difference in vorticity values between the two subvortices (Fig. 11).

As G-1 became a larger, deeper, and more intense subvortex than G-2, it began to exact an apparent direct influence on G-2's behavior. Figure 13 illustrates the evolution of the location of G-2 relative to G-1 during the time period that the two subvortices were apparent within mesovortex G. During the first half of their lifespans, G-2 showed very little consistent motion relative to G-1, limited to noise in the determination of the center points of the subvortices. After 0341 UTC, however, G-2 begins to move in a distinct cyclonic fashion around and toward G-1, culminating in the merger of the two subvortices back into a single, large mesovortex after 0359 UTC (Fig. 13). There is also some suggestion of possible trochoidal oscillations (Kuo 1969) in the path of G-2, although the first-order analysis and relative low 0.5° temporal resolution preclude a definitive diagnosis of such behavior. This acceleration and inward motion of G-2 toward G-1 begins coincident with the substantial intensity changes noted in the subvortices in Fig. 11, and seems to mirror the behavior of satellite tornadoes around larger parent tornadoes (e.g. Wurman and Kosiba 2013), only at the mesovortex scale. Implications of this mesovortex split and the characteristics of the two subvortices are further discussed in Section 5.

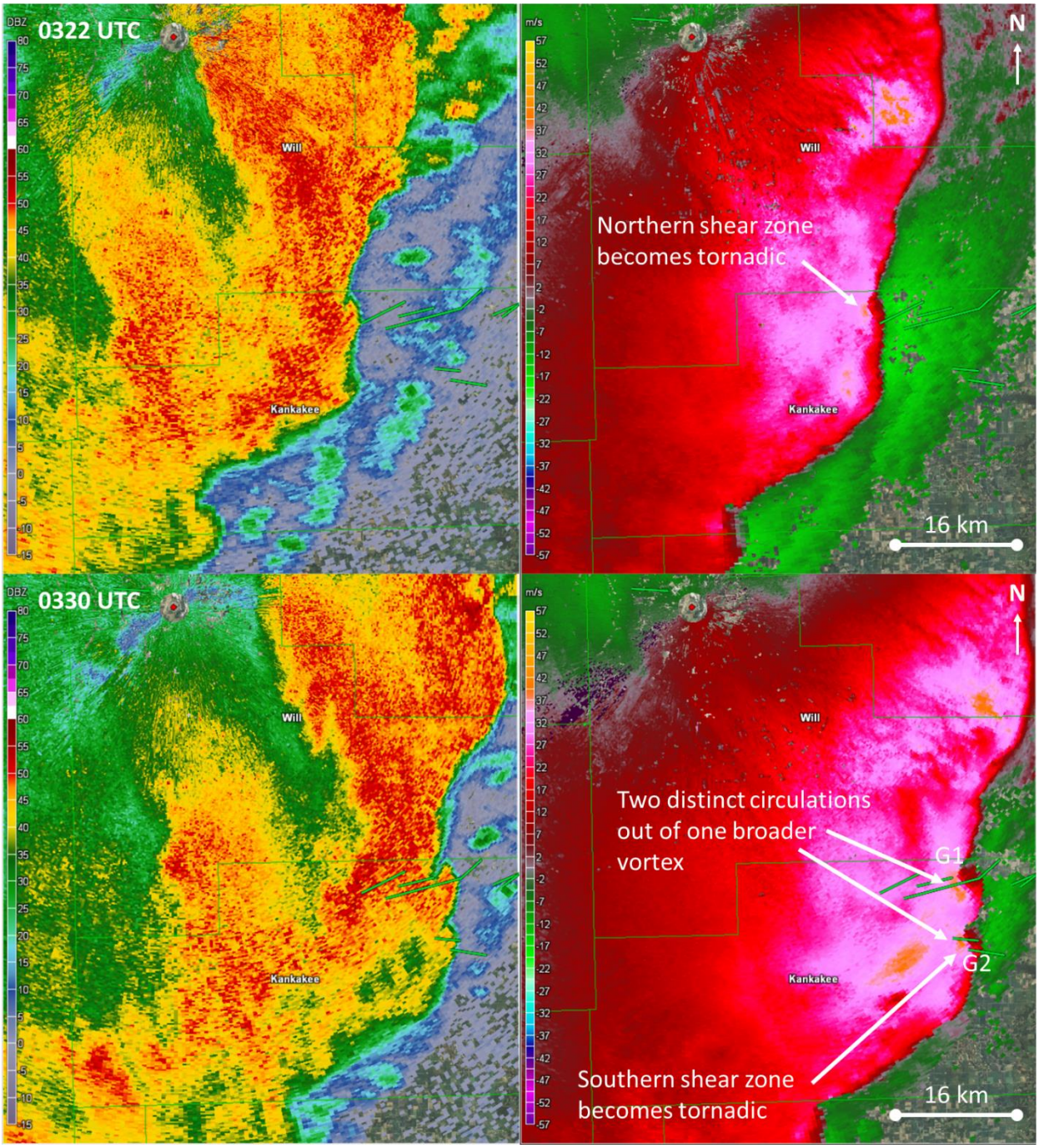

Fig. 8: As in Fig. 6 at 0322 UTC (top) and 0330 UTC (bottom) on 1 July 2014, showing G-1 and G-2 as they became tornadic.

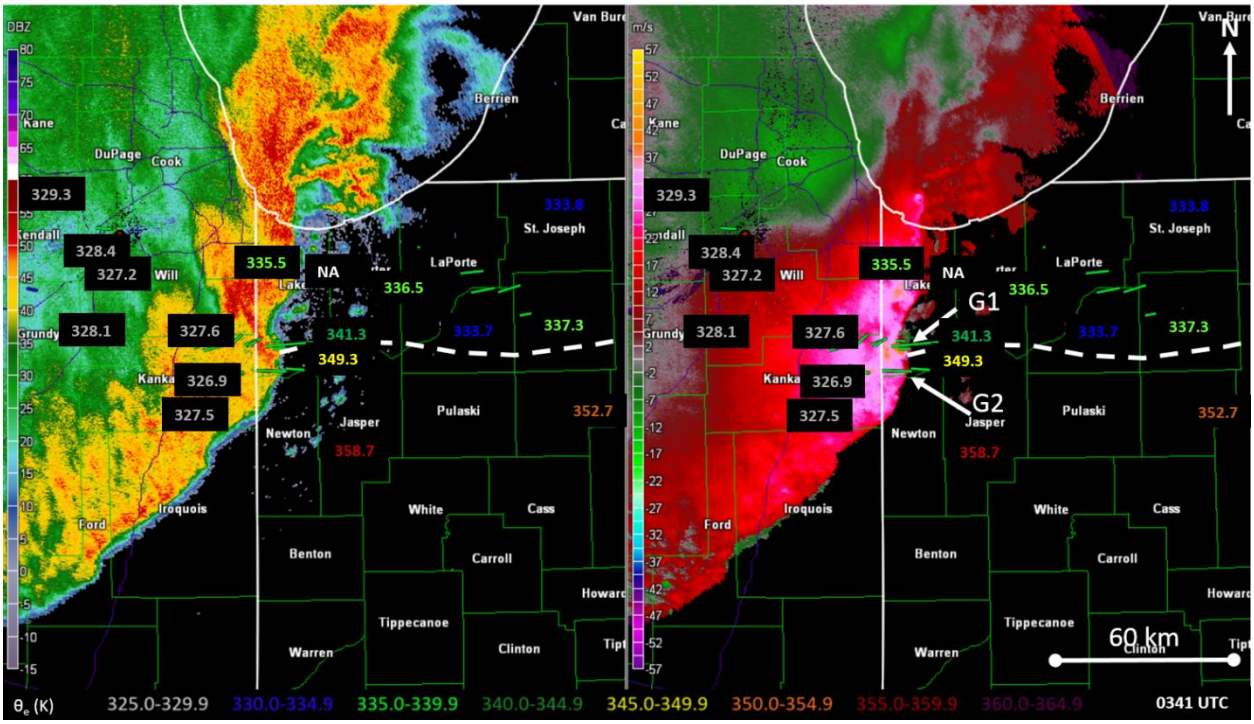

Fig. 9: As in Fig. 5 for 0341 UTC 1 July 2014. G-1 is propagating along the thermal boundary at this time.

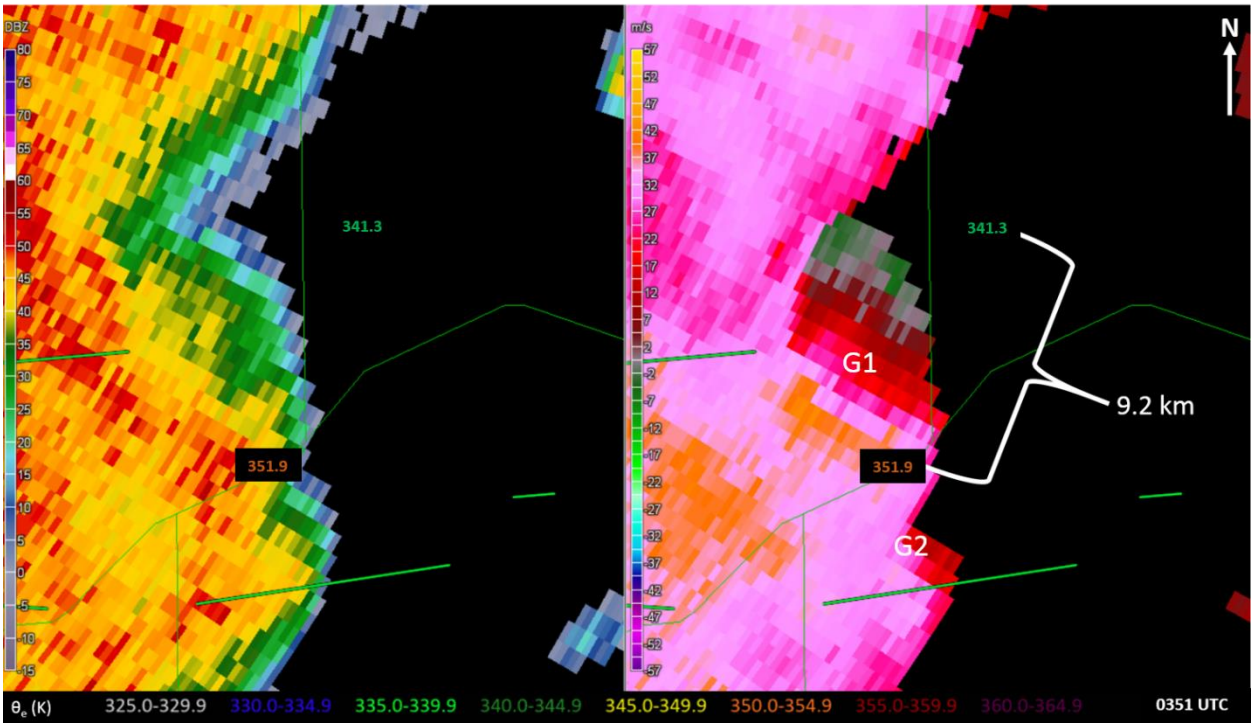

Fig. 10: As in Fig. 5 at 0351 UTC 1 July 2014, with a zoomed-in focus at two cooperative observer sites in northwest Indiana. The two sites are on opposite sides of the thermal boundary and are 9.2 km apart. A θ_e change of 10.6 K is evident. Also noted is the apparent location of G-1 along the thermal boundary. The southern observer measured a wind gust to 38 m s^{-1} (86 MPH) along the southern periphery of G-1 before power to the station failed. Damage was rated high-EF1 intensity in this area.

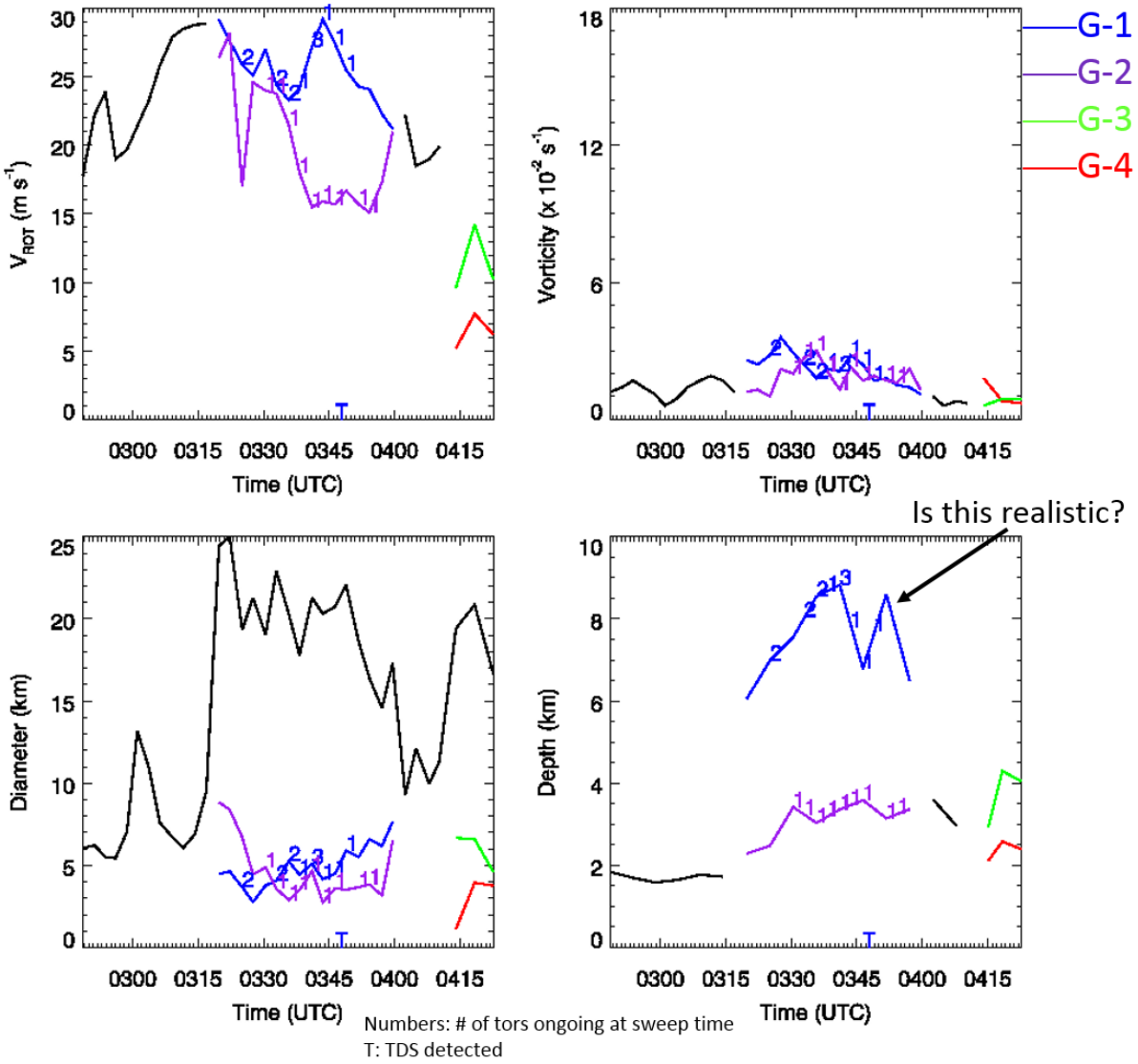

Fig. 11: Time-series plots of rotational velocity (V_{ROT}), vorticity (ζ; upper-right), diameter (lower-left), and depth (lower-right) from the KLOT WSR-88D from 0248 UTC to 0423 UTC 1 July 2014, showing the evolution of variables during the lifetime of mesovortex G.

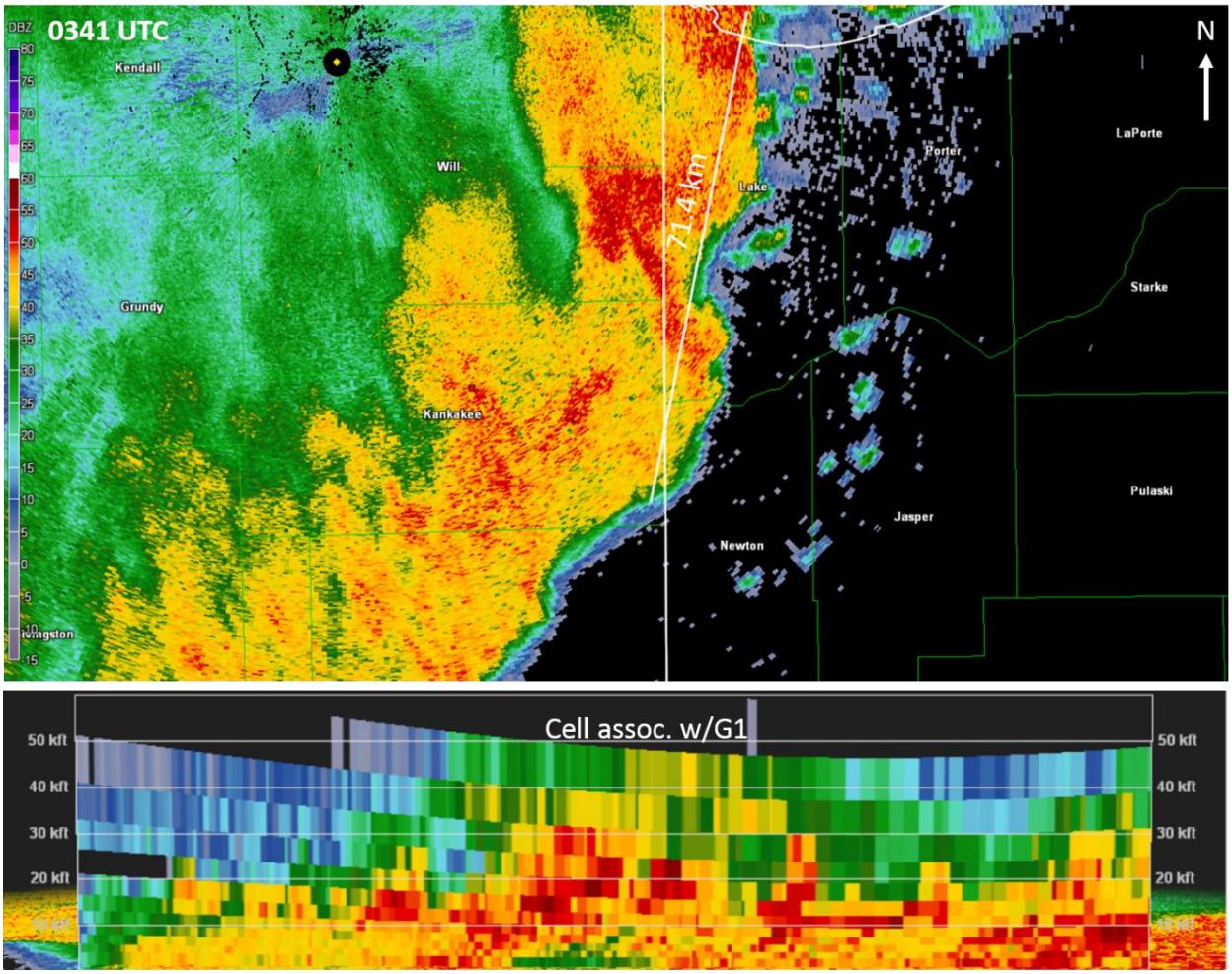

Fig. 12: Cross-section of Z_e from the KLOT WSR-88D at 0341 UTC (below), showing the height of the Z_e core for the cell associated with G-1 versus the rest of the surrounding QLCS. Cross-section was taken through region of line indicated in the PPI (above).

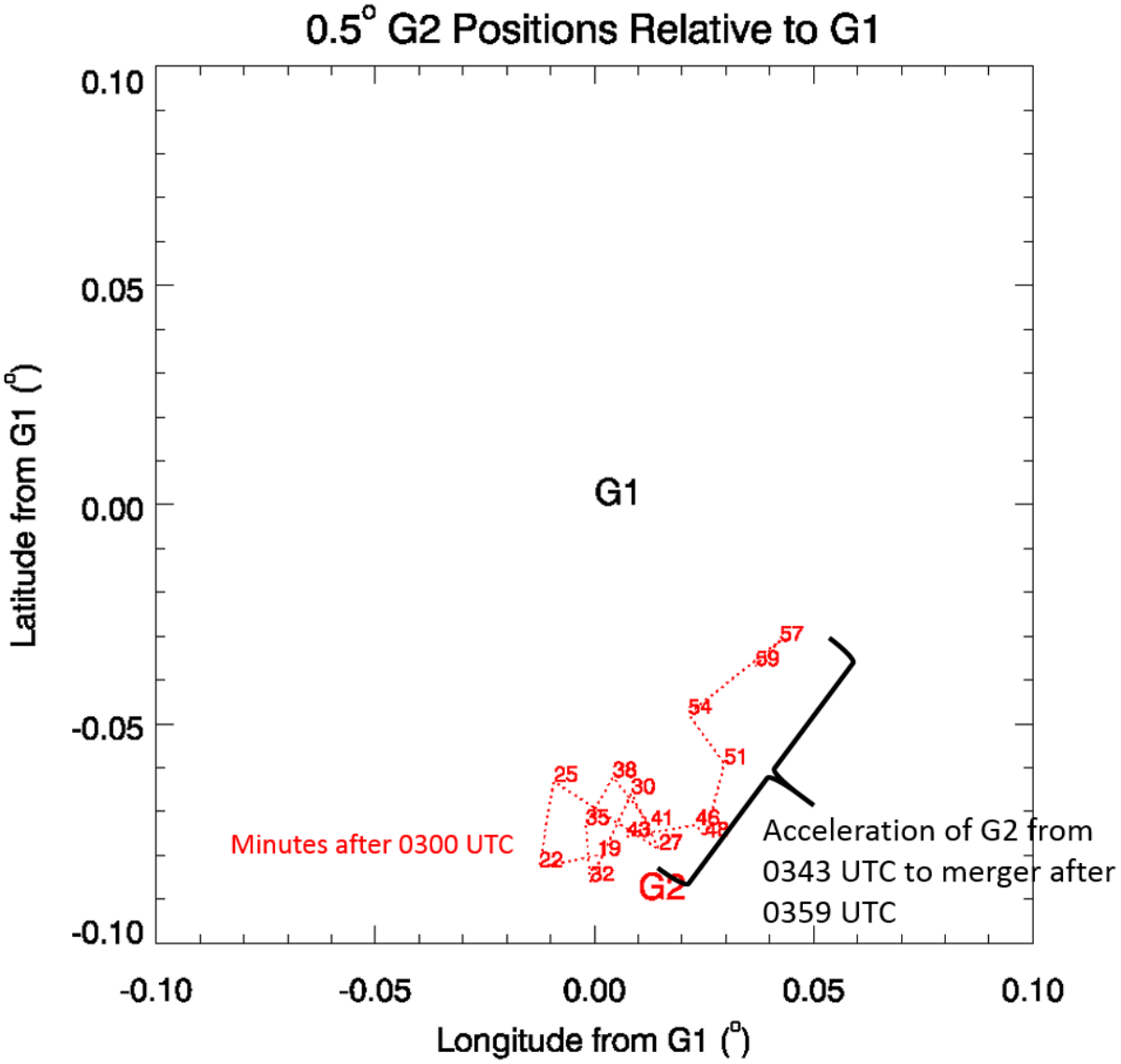

Fig. 13: Plot of the position of G-2 relative to G-1 between 0319 UTC and 0359 UTC 1 July 2014.

3. The Satellite Natures of Mesovortices U, V, and W around Mesovortex K

Farther to the east across northern Indiana, the nature of the mesovortices produced by the second derecho transitioned from 3-5 simultaneous large, long-lived mesovortices to numerous smaller, shorter-lived vortices embedded amongst a few longer-lived circulations. Many of these mesovortices formed in close proximity to each other, leading to a number of unusual interactions between mesovortices. The most remarkable interaction between mesovortices was noted between long-lived mesovortex K and the shorter-lived mesovortices U, V, and W across north-central Indiana (Fig. 14). Mesovortex U formed at approximately 0444 UTC approximately 6.7 km south-southwest (189°) of mesovortex K, while mesovortices V and W both formed at approximately 0448 UTC approximately 5.0 km east-northeast (68°) and 6.1 km south (185°) of mesovortex K, respectively (Fig. 15). As the second derecho continued to propagate to the east, the positions of mesovortices U, V, and W relative to mesovortex K shifted in a counterclockwise direction. By 0452 UTC, mesovortex U was approximately 3.0 km east-southeast (102°) of mesovortex K, mesovortex V was 2.8 km northeast (48°) of mesovortex K, and mesovortex W was 3.4 km southeast (160°) of mesovortex K (Fig. 16). After 0452 UTC, mesovortices U and V began to be absorbed into mesovortex K, with U located approximately 1.8 km east-northeast (66°) of mesovortex K and V located approximately 3.4 km north (356°) of K (Fig. 17). By 0501 UTC, U and V are absorbed into K, and mesovortex K is about to be absorbed by K (Fig. 17).

To better understand the motions of U, V, and W around mesovortex K, the positions of U, V, and W were plotted relative to K in Fig. 18. When plotted in a Lagrangian framework, the satellite nature of mesovortices U, V, and W to K becomes readily apparent. Mesovortex U begins to the south-southwest of mesovortex K and ends to the east-northeast of K; mesovortex V begins to the east-northeast of K and ends just west of due north of K, and mesovortex W begins and ends to the south of K but exhibits a northeastward motion for much of its life and moves much closer to K overall. To the authors' knowledge, this is the first documented case of satellite mesovortex documentation in a QLCS. Implications of these observations are discussed in Section 5.

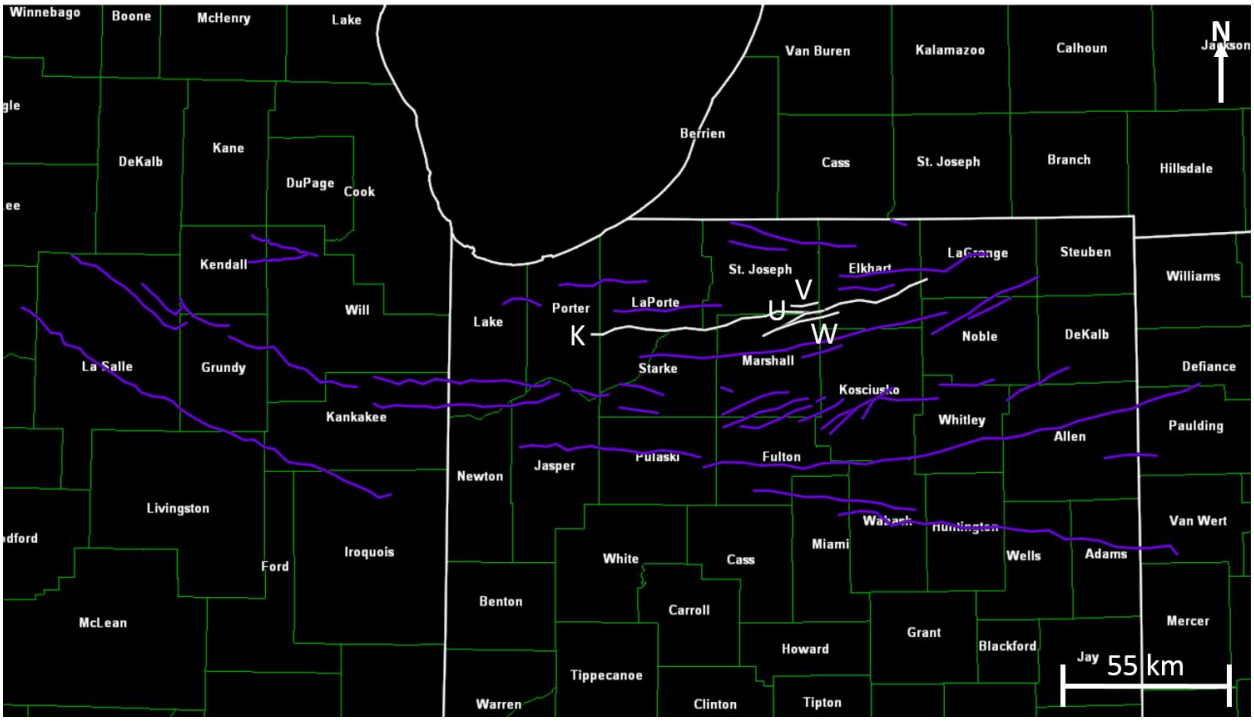

Figure 14: As in Fig. 4 for mesovortices K, U, V, and W.

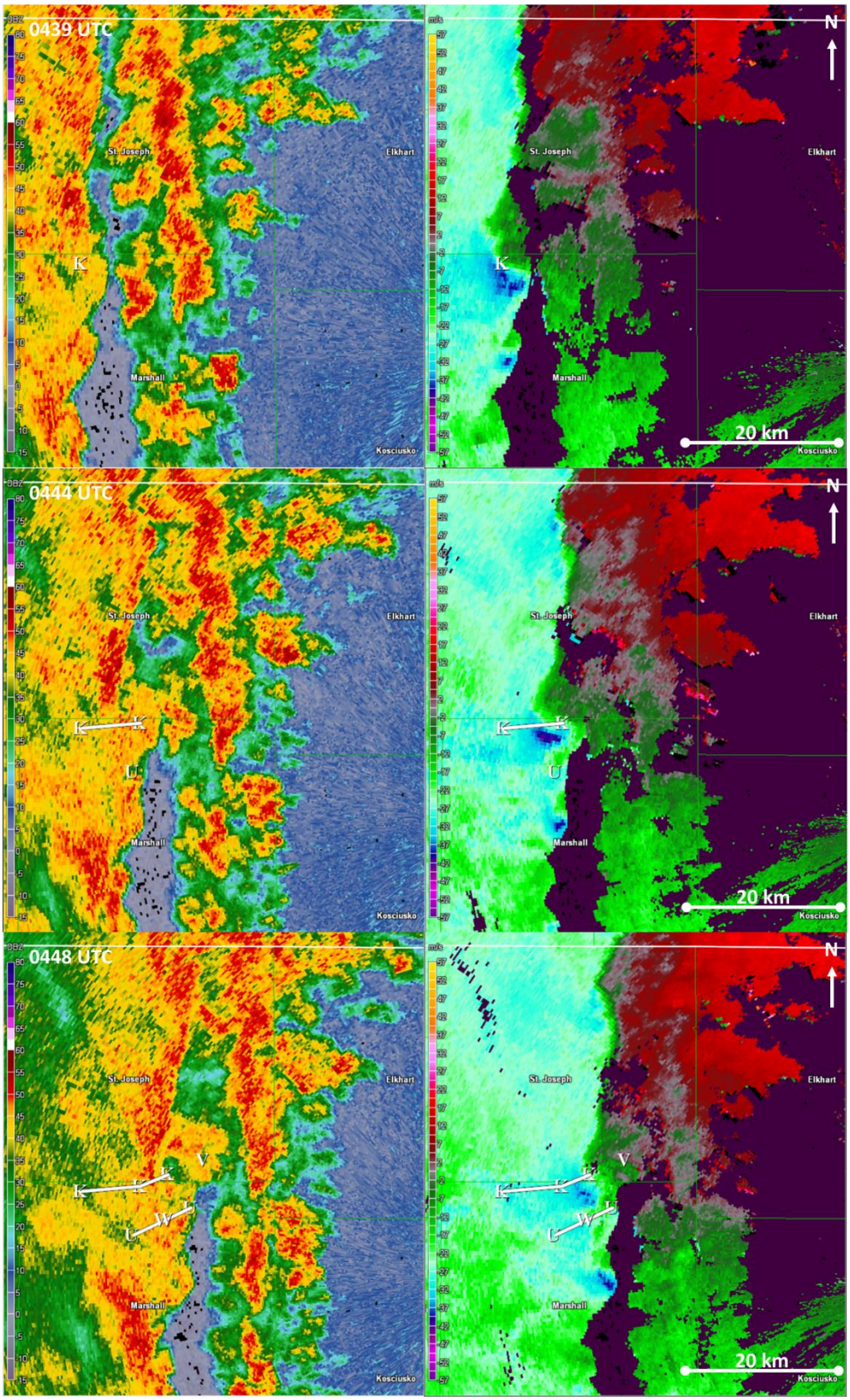

Fig. 15: 0.5° PPI of Z_e (left) and V_r (right) from the Northern Indiana (KIWX) WSR-88D radar at 0439 UTC (top), 0444 UTC (middle), and 0448 UTC (bottom) on 1 July 2014, illustrating the development of mesovortices U, V, and W.

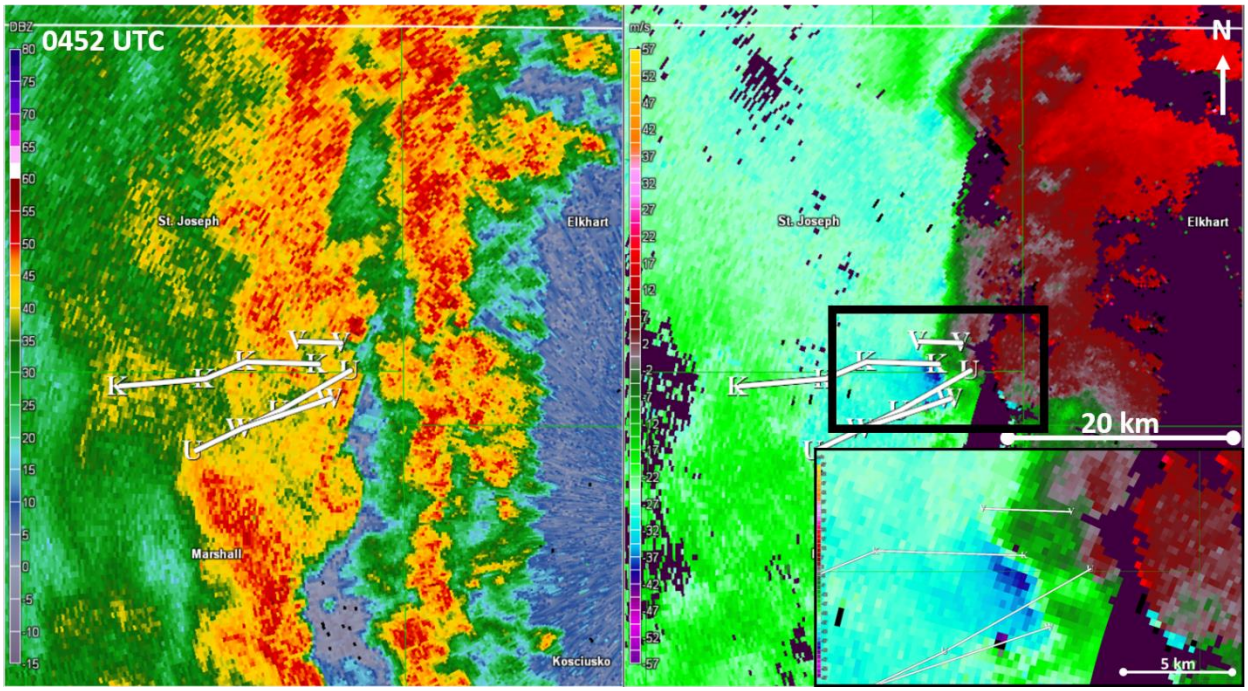

Fig. 16: As in Fig. 15 at 0452 UTC on 1 July 2014, showing the locations of mesovortices K, U, V, and W, with a zoomed-in view of the mesovortices in the inset.

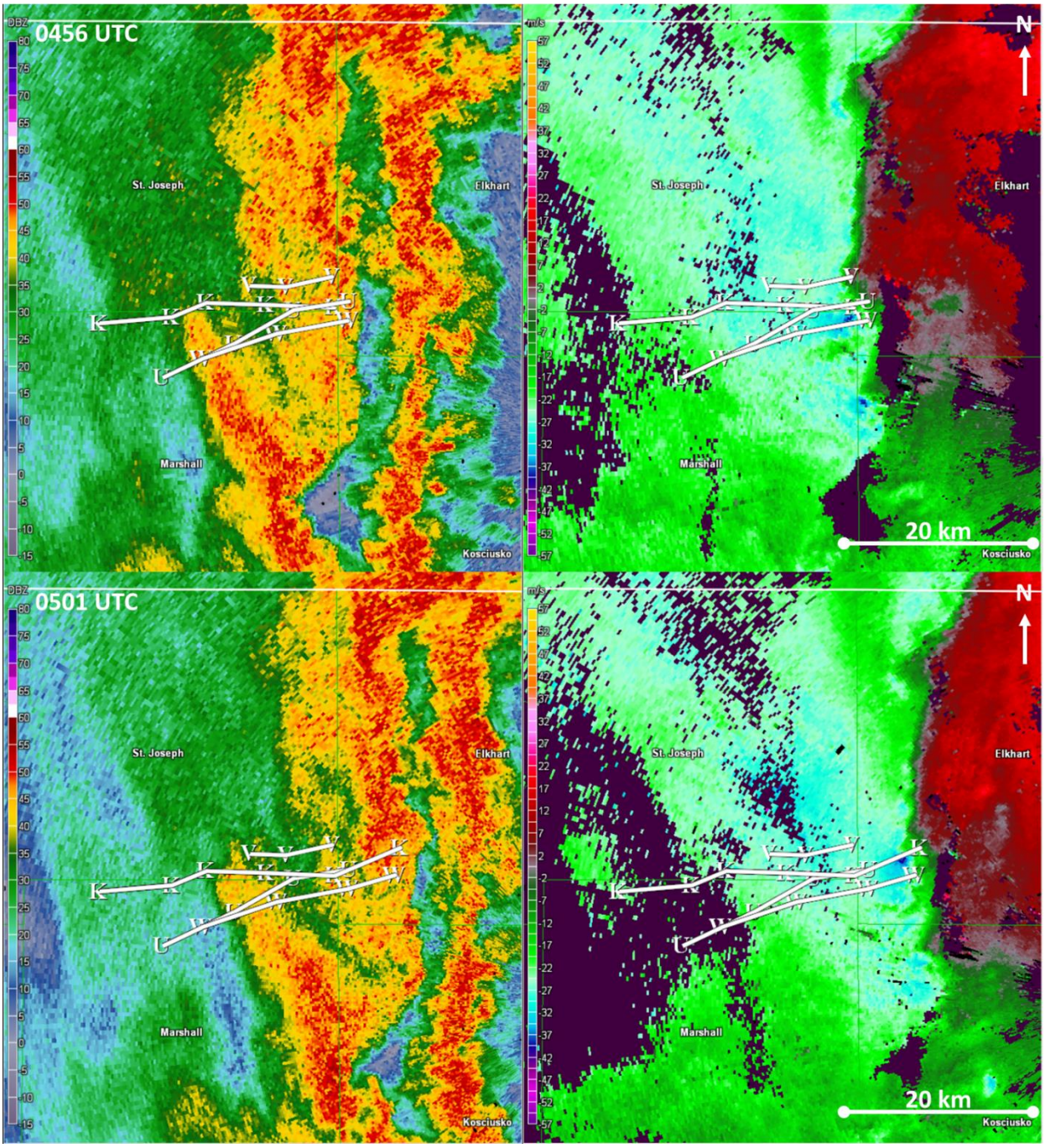

Fig. 17: As in Fig. 15 at 0456 UTC (top) and 0501 UTC (bottom) on 1 July 2014, showing the mergers of mesovortices U, V, and W into mesovortex K.

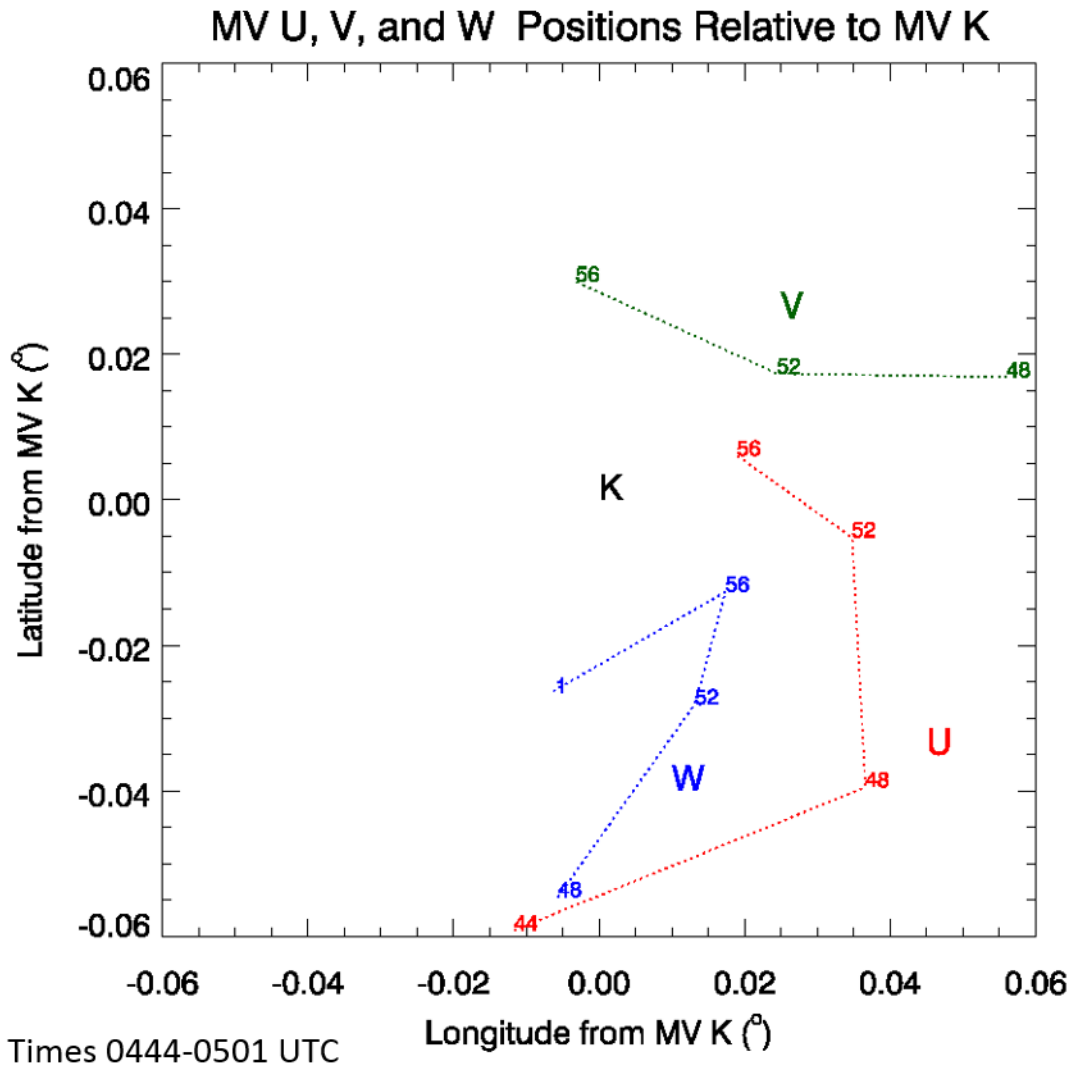

Fig. 18: Plot of the center points of mesovortices U, V, and W relative to the center point of mesovortex K, showing the satellite nature of U, V, and W to K.

4. The Merging of Multiple TDSs into an Single Debris Cloud

As the interactions between mesovortices K, U, V, and W were ongoing, the second derecho was producing numerous additional mesovortices to the south. Four of these mesovortices, named R, T, Z, and AA in the nomenclature, formed in extremely close proximity to each other, with a range of approximately 2.7 km to 3.9 km between mesovortices (Fig. 19). Figure 20 illustrates the locations of R, T, and Z, along with a decaying additional mesovortex (Q) at 0452 UTC on 1 July 2014. None of the mesovortices are associated with dual-polarimetric TDSs in Fig. 20. By 0456 UTC (Fig. 21), mesovortices R and T are beginning to dissipate in V_r, but both show TDS signatures (using a crosspolar correlation coefficient (ρ_{hv}) constraint of 0.9 due to a lack of hail observed in the second derecho), with the two TDS signatures beginning to merge into one. Mesovortex Z also shows a clear TDS signature at 0456 UTC. Another couplet (mesovortex AA) also appears ahead of decaying mesovortex T at 0456 UTC. By 0501 UTC (Fig. 22), the couplets of mesovortices R and T have dissipated, but downstream is lower than at 0456 UTC and now collocated with mesovortex AA. The debris from R, T, and AA are also now merged with the debris signature of the still-active mesovortex Z, creating one large, elongated debris cloud, or TDS "wall". The implications of this complex dual-polarimetric evolution on severe weather warning operations is discussed in Section 5.

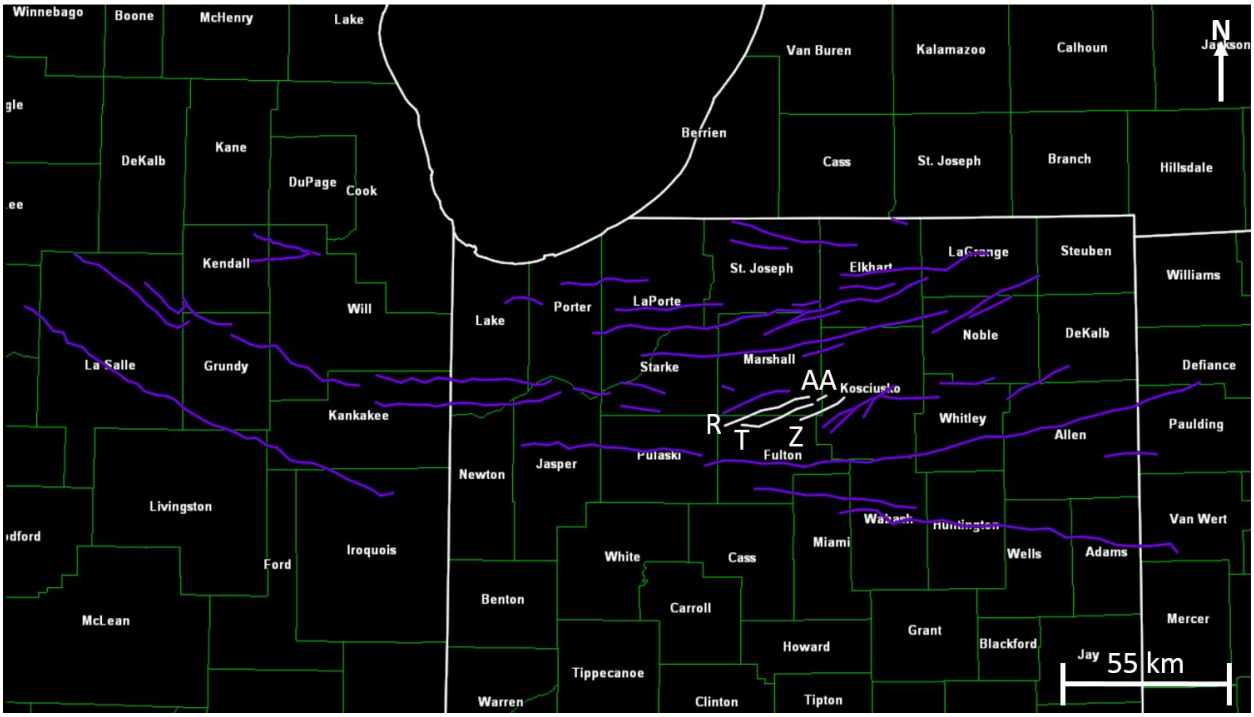

Fig. 19: As in Fig. 4 for mesovortices R, T, Z, and AA.

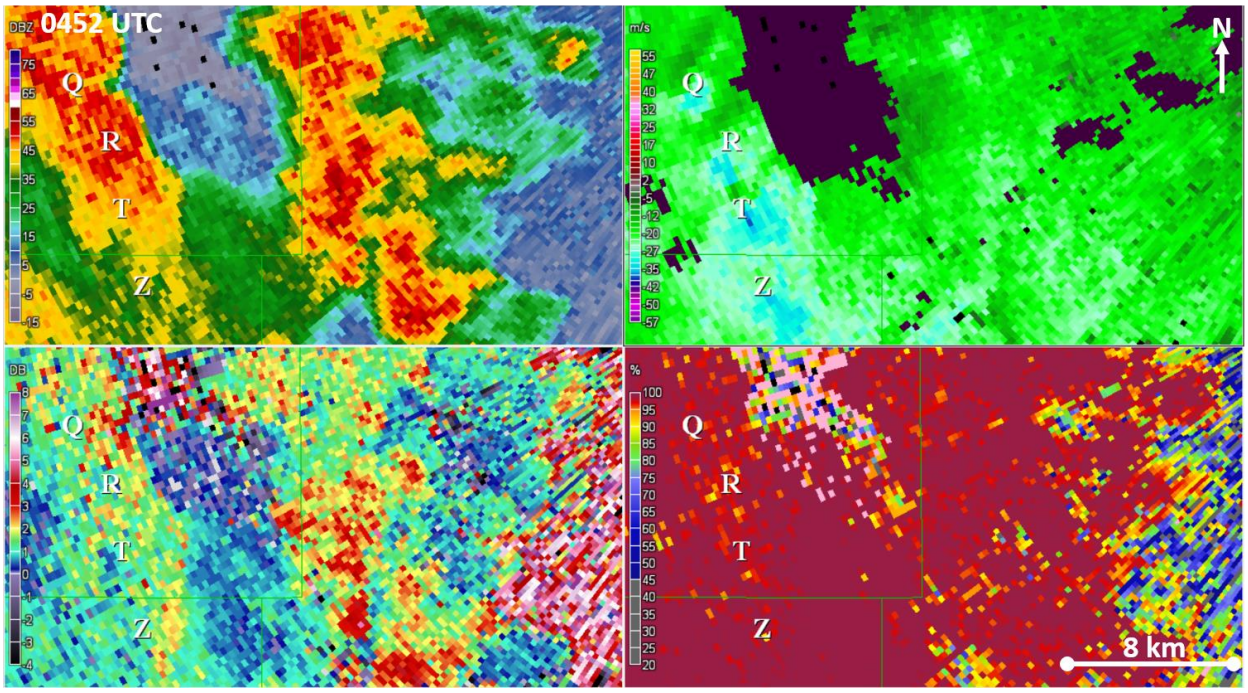

Fig. 20: Four-panel PPI plot of Z_e (upper-left), V_r (upper-right), differential reflectivity (Z_{DR}, lower-right), and crosspolar correlation coefficient (ρ_{hv}, lower-right) from the KIWX WSR-88D radar at 0452 UTC on 1 July 2014, showing the couplets of mesovortices Q, R, T, and Z tightly spaced together.

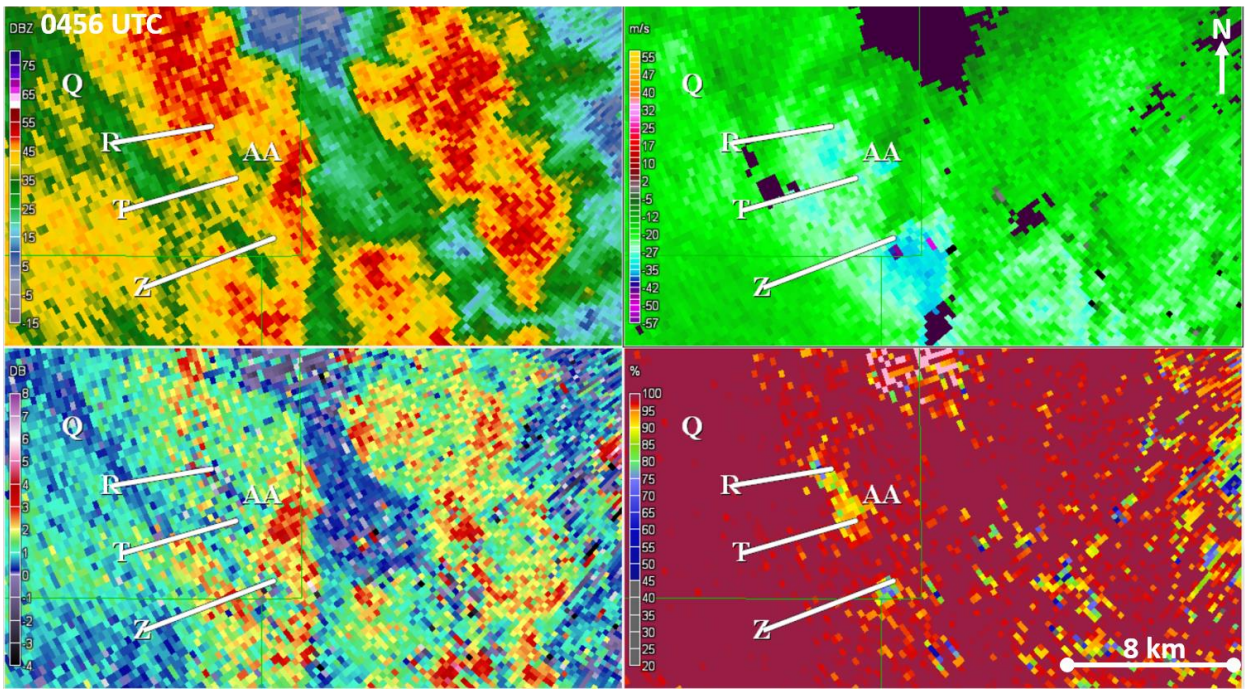

Fig. 21: As in Fig. 20 at 0456 UTC 1 July 2014. TDSs are now evident for mesovortices R, T, and Z, with the signatures for R and T beginning to merge together. Mesovortex AA is now also apparent at this time.

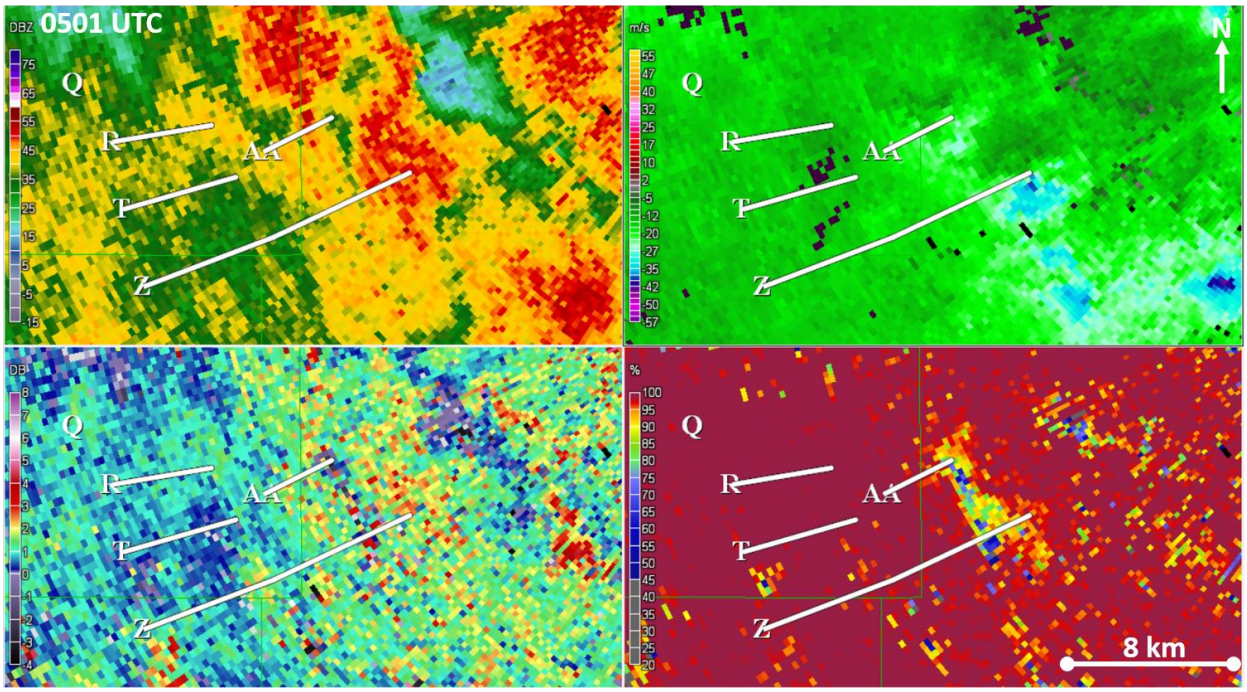

Fig. 22: As in Fig. 20 at 0501 UTC 1 July 2014. TDSs from mesovortices R, T, Z, and AA have blended into one elongated "wall" of debris by this time.

5. Discussion and Future Work

The mesovortices of the second 30 June – 1 July 2014 Midwestern derecho present a number of problems for both the research and operational meteorology community. These problems can best be summarized through the following questions:

1) Why did mesovortex G split into two subvortices, and did this split modulate the tornado production of the mesovortex?
2) Was there a fundamental change in mesovortex genesis mechanisms from northern Illinois, where there were a handful of larger, longer-lived mesovortices, to northern Indiana, where there were many more mesovortices ongoing simultaneously but the vortices were smaller and usually shorter-lived that those in Illinois?
3) Did the depth of subvortex G-1 result from a superposition of low-level and mid-level vortices, or did G-1 attain a supercell mesocyclone-like structure?
4) How do mesovortices acquire satellite behavior? Is this behavior similar to satellite tornadoes, multiple-vortex tornadoes, or is a completely different mechanism at work?
5) Are satellite mesovortices truly uncommon phenomena, or have past radar data simply not been interrogated sufficiently to notice them?
6) How can the issue of merging TDSs be addressed in the operational community, where such signatures under high-pressure situations with widespread severe weather activity ongoing can cause potential for confusion given deviation from the standard TDS concept?

In addition to addressing the above questions, future work will continue on detailing additional observations related to mesovortices observed in the second derecho, including a close-up detection of a tornado by the KLOT WSR-88D radar, an instance of a binary (Fujiwhara) interaction captured by the Chicago-Midway International Airport (KMDW) TDWR radar with one-minute lowest-tilt temporal resolution, and at least one additional case of satellite behavior of one mesovortex around another. Future work will also include an in-depth analysis of TDS characteristics, including size and depth, for each TDS observed during the event. Other work will include a large-scale analysis of dual-polarimetric radar data of the second QLCS, linking radar characteristics to damage survey information, particularly for mesovortex G, and further investigation into the meteorological characteristics of the second derecho, including the pre-storm environment and propagation mode of the QLCS.

REFERENCES

Atkins, N. T., and J. M. Arnott, R. W. Przybylinski, R. A. Wolf, and B. D. Ketcham, 2004: Vortex Structure and Evolution within Bow Echoes. Part I: Single-Doppler and Damage Analysis of the 29 June 1998 Derecho. *Mon. Wea. Rev.*, **132**, 2224–2242.

Atkins, N. T., and M. St. Laurent, 2009: Bow Echo Mesovortices. Part I: Processes That Influence Their Damaging Potential. *Mon. Wea. Rev.*, **137**, 1497–1513.

Friedlein, M., and R. Castro, E. Lenning, A. W. Lyza, and K. R. Knupp, 2015: Evolution of the 30 June 2014 Double Derecho Event in Northern Illinois & Northwest Indiana. Preprints, *27th Conference On Weather Analysis And Forecasting/23rd Conference On Numerical Weather Prediction*, Chicago, IL, Amer. Meteor. Soc.

Fujita, T., 1981: Tornadoes and Downbursts in the Context of Generalized Planetary Scales. *J. Atmos. Sci.*, 38, 1511–1534.

Kuo, H. L., 1969: Motions of Vortices and Circulating Cylinder in Shear Flow with Friction. *J. Atmos. Sci.*, **26**, 390–398.

Lenning, E., and R. Castro, M. Friedlein, A. W. Lyza, and K. R. Knupp, 2015: Storm Scale Meteorological Processes in the 30 June 2014 Double Derecho Event. Preprints, *27th Conference On Weather Analysis And Forecasting/23rd Conference On Numerical Weather Prediction*, Chicago, IL, Amer. Meteor. Soc.

McDonald, J. R., G. S. Forbes, and T. P. Marshall, 2004: The enhanced Fujita (EF) scale. *Preprints, 22nd Conf. on Severe Local Storms*, Hyannis, MA, Amer. Meteor. Soc., 3B.2. [Available online at https://ams.confex.com/ams/11aram22sls/techprogram/paper_81090.htm]

NWS Chicago, cited 2015: Two Separate Derecho Events on June 30, 2014. Available online at [http://www.weather.gov/lot/2014Jun30_Two_Derecho]

Ryzhkov, A. V., T. J. Schuur, D. W. Burgess, D. S. Zrnic, 2005: Polarimetric Tornado Detection. *J. Appl. Meteor.*, **44**, 557–570.

Schultz, C. J., and Coauthors, 2012: Dual-Polarization Tornadic Debris Signatures Part I: Examples and Utility in an Operational Setting. *Electronic J. Operational Meteor.*, **13** (9), 120−137.

Schultz, C. J., and Coauthors, 2012: Dual-polarization tornadic debris signatures Part II: Comparisons and caveats. *Electronic J. Operational Meteor.*, **13** (10), 138−150.

Storm Prediction Center, cited 2015: SPC National Severe Weather Database Browser: Online SeverePlot 3.0. Available online at [http://www.spc.noaa.gov/climo/online/sp3/plot.php]

Wakimoto, R. M., H. V. Murphey, C. A. Davis, and N. T. Atkins, 2006: High Winds Generated by Bow Echoes. Part II: The Relationship between the Mesovortices and Damaging Straight-Line Winds. *Mon. Wea. Rev.*, **134**, 2813–2829.

Weisman, M. L., and R. J. Trapp, 2003: Low-Level Mesovortices within Squall Lines and Bow Echoes. Part I: Overview and Dependence on Environmental Shear. *Mon. Wea. Rev.*, **131**, 2779–2803.

Wheatley, D. M. and R. J. Trapp, 2008: The Effect of Mesoscale Heterogeneity on the Genesis and Structure of Mesovortices within Quasi-Linear Convective Systems. *Mon. Wea. Rev.*, **136**, 4220–4241.

Wurman, J., and K. Kosiba, 2013: Finescale Radar Observations of Tornado and Mesocyclone Structures. *Wea. Forecasting*, **28**, 1157–1174.